Chemical Engineering Journal 541 (2026) 177622

Contents lists available at ScienceDirect

Chemical Engineering Journal

journal homepage: www.elsevier.com/locate/cej

Enhanced passive micromixing via asymmetric height-variable micropillar arrays at low Reynolds numbers

Azeez Bakare [a], Prabuddha De Saram [a], Hongjie An [a,b], Nam-Trung Nguyen [a,c,*], Navid Kashaninejad [a,c,*]

[a] Queensland Quantum and Advanced Technologies Research Institute, Griffith University, 170 Kessels Road, Nathan, QLD, 4111, Australia
[b] School of Environment and Science, Griffith University, 170 Kessels Road, Nathan, QLD, 4111, Australia
[c] School of Engineering and Built Environment, Griffith University, 170 Kessels Road, Nathan, QLD, 4111, Australia

ARTICLE INFO

Keywords:
Chaotic advection
Diffusion
Micromixer
Micropillar
Mixing efficiency

ABSTRACT

Efficient mixing in microfluidic systems is essential for many biological, chemical, and diagnostic applications, yet it remains challenging at low Reynolds numbers, where laminar flow and diffusion-limited transport dominate. Here, we investigate passive micromixing as a function of systematic micropillar height variation along the flow direction over a Reynolds number range of 0.1–10. Four micromixer configurations are examined, including a plain channel without micropillars and three micropillar arrays with uniform, half-square-wave, and backward sawtooth height profiles, implemented in a device comprising two mixing chambers. Mixing efficiency, efficiency ratio, and performance index are quantified experimentally and numerically in both chambers. All micropillar configurations outperform the plain design, demonstrating the effectiveness of three-dimensional geometric modulation for low-*Re* mixing. Among the tested designs, the asymmetric backward sawtooth configuration provides the most robust enhancement by promoting transverse flow components and sustained interfacial stretching. Mixing efficiency in the downstream chamber consistently exceeds that in the upstream chamber due to cumulative hydrodynamic development and stronger recirculation. The backward sawtooth design achieves a maximum mixing efficiency of approximately 98% at a Reynolds number of about 0.9, while efficiency ratios in the downstream chamber reach up to 1.6 relative to the plain configuration. At a Reynolds number of 0.1, the performance index of the uniform micropillar design is nearly four times higher than that of the plain channel. The close agreement between experimental and numerical results demonstrates that height-graded, asymmetric micropillar arrays offer an energy-efficient and scalable strategy for high-performance passive micromixing under diffusion-dominated conditions, with direct relevance to lab-on-a-chip systems.

1. Introduction

Micromixers support a wide range of applications, including lab-on-a-chip and organs-on-chip systems involving cell handling and conditioning [1,2], biomedical and pharmaceutical microfluidic devices [3], and water treatment and environmental monitoring [4]. They operate through either active or passive mechanisms [5]. When micromixers are appropriately designed and optimised for a specific application, they can greatly improve process efficiency and product quality. However, efficient mixing remains difficult at low Reynolds numbers, where the flow is primarily laminar and mass transport is mainly governed by diffusion [6]. Under such conditions, achieving complete diffusive mixing often requires a lengthy channel, thereby increasing device footprint and limiting compact system integration [7].

The material selected and the fabrication method used strongly influence the quality, cost, reproducibility, and practical applicability of micromixers. Different materials have distinct material properties, including thermal, chemical, and mechanical characteristics, which affect their suitability for use in microfluidic systems [8–10]. Although material selection does not usually improve mixing directly, it determines how accurately and reliably complex surface and three-dimensional (3D) geometric features can be fabricated, which in turn affects mixing performance. For example, Mondal et al. reported a rapid fabrication approach for polydimethylsiloxane (PDMS)-based wavy

* Corresponding authors at: Queensland Quantum and Advanced Technologies Research Institute, Griffith University, 170 Kessels Road, Nathan, QLD, 4111, Australia.
E-mail addresses: nam-trung.nguyen@griffith.edu.au (N.-T. Nguyen), n.kashaninejad@griffith.edu.au (N. Kashaninejad).

https://doi.org/10.1016/j.cej.2026.177622
Received 30 January 2026; Received in revised form 18 May 2026; Accepted 21 May 2026
Available online 26 May 2026
1385-8947/© 2026 The Authors. Published by Elsevier B.V. This is an open access article under the CC BY license (http://creativecommons.org/licenses/by/4.0/).

micromixers using carbon dioxide laser-milled polymethyl methacrylate (PMMA) moulds combined with soft lithography, allowing flexible prototyping of efficient mixer designs [9].

Micromixer performance is strongly influenced by geometric design. In addition to channel layout and pillar shape, 3D geometric features offer further opportunities to control flow fields under laminar conditions, although their systematic experimental investigation remains limited [11]. Common layouts such as T, Y, Tesla, serpentine, and spiral channels, as well as channels incorporating micropillars with various shapes, including hexagonal, square, and circular cross sections, have been widely investigated to enhance micromixing [12–15]. Among these approaches, micropillar arrays have gained increasing attention due to their ability to shape flow, promote interface deformation, and induce transverse motion in otherwise laminar streams. Representative examples include magnetically actuated micropillars used to improve mixing for glucose detection [16] and diamond-shaped pillars incorporated into splitting and recombination channels, optimised using artificial neural networks coupled with computational fluid dynamics (CFD) [17]. More broadly, studies on passive micromixing at low Reynolds numbers (*Re*) have shown that geometric asymmetry and 3D flow modulation can improve interfacial deformation and transverse transport beyond diffusion alone [18,19]. Classic examples include staggered herringbone-based designs and other geometry-optimised micromixers in which small structural modifications generate secondary flow, increase interfacial area, and improve downstream homogenisation [18–20]. Recent studies have continued to use this principle through asymmetrically arranged Tesla micromixers [21], optimised three-dimensional passive architectures [22], and zigzag obstacle-assisted layouts [23], confirming that geometric non-uniformity remains an active strategy for low-*Re* passive mixing. However, these designs do not clarify the comparative role of height-variable asymmetric micropillar arrays within a single passive platform, particularly through experimental validation.

Without micropillars, achieving mixing efficiencies of about 80–95% generally requires longer channels, more complex geometries, or operation at intermediate to high Reynolds numbers. For example, splitting-and-recombining micromixers with lengths of 7 to 11 mm have been reported to achieve mixing efficiencies ranging from 70 to 99% at Reynolds numbers between 1 and 150 [24,25], while spiral micromixers with lengths of approximately 28 mm can achieve mixing efficiencies close to 96%. In contrast, micropillar arrays can achieve similar mixing efficiencies of 97–99% within much shorter channel lengths of 6–6.5 mm and with shorter mixing times [26]. This highlights the importance of geometric features that increase interfacial area and maintain transverse transport, particularly at low *Re*.

The performance of micropillar-based micromixers depends on several factors, including the number of pillars, their shape, arrangement, height, spacing, and material stiffness. Previous studies have explored a range of design strategies, such as interface maximising pillar configurations optimised using FlowSculpt methods [27], comparisons between quadratic and hexagonal arrays with varying spacing densities [28], slanted-arrowhead arrangements [26], and the influence of gaps, pillar shapes, and flow rates on mixing behaviour [29]. Recent studies have also examined the effect of micropillar height in actively actuated systems, such as acoustofluidic micromixers, where pillar height is optimised to enhance acoustic streaming [11]. However, these approaches rely on external actuation and consider arrays of uniform-height pillars, leaving the role of spatially varying pillar-height profiles in purely passive micromixing unexplored. The technical distinction of the present design lies in combining asymmetric chamber geometry with height-variable micropillar arrays within a single micromixer platform. Unlike pillar-free or uniformly pillared layouts, the proposed half-square-wave (HSW) and backward-sawtooth (BST) configurations introduce deliberate geometric non-uniformity, which promotes progressive flow redistribution, interfacial stretching, and transverse transport at low *Re* [18–20]. Recent studies have continued to use this principle in asymmetrically arranged Tesla micromixers [30], optimised three-dimensional passive designs [22], and experimentally validated zigzag obstacle-assisted layouts [23]. They showed that geometric non-uniformity remains an active strategy for passive mixing at low Reynolds numbers. However, these designs still do not clarify the comparative role of height-variable asymmetric micropillar arrays within a single passive platform, particularly through controlled experimental comparison under the same geometric framework.

To address these limitations, the present study examines strategically arranged micropillar arrays with intentionally varied pillar heights along the flow direction, compared with a no-pillar baseline design. By exploiting molecular diffusion at Reynolds numbers between 0.1 and 1 and chaotic advection at Reynolds numbers between 1 and 10, the micromixer is evaluated over a low-to-intermediate Reynolds number range of 0.1 to 10. Numerical simulations and experimental measurements were used to evaluate the mixing efficiency and performance index, allowing a systematic assessment of the effect of structured height variation and geometric asymmetry on passive micromixing at low *Re*. In addition, the study compares no-pillar, uniform, and height-variable asymmetric configurations within the same geometric platform, allowing the effect of controlled micropillar-height modulation to be isolated more clearly than in previous passive micromixer designs.

2. Materials and methods

2.1. Micromixer design and geometry

Fig. 1a shows the SolidWorks (2024) design of the micromixer, consisting of two 2.8 mm inlets feeding a Y-junction, two identical mixing chambers with dimensions of 3 mm × 3 mm, and a 2 mm outlet. Two chamber configurations are investigated. The first is a no-pillar configuration (NM) with a chamber depth of h = 200 μm. The second consists of micropillar array configurations with an overall chamber depth of H = 1 mm.

Three 10 × 10 arrays of conical micropillars are examined. The conical geometry results from the laser machining process. All arrays share a pillar diameter of 120 μm and a pitch of 300 μm but differ in their height profiles and spatial arrangements. These include a uniform-height array (U) with a constant pillar height of 800 μm, a half-square-wave (HSW) height profile with pillar heights varying between 500 and 800 μm, and a backward sawtooth (BST) height profile with pillar heights also varying between 500 and 800 μm. The HSW and BST designs introduce systematic spatial height variation within a single array along the flow direction. Figs. 1b, c, and d illustrate the pillar arrangements for the three design configurations.

2.2. Design rationale for micropillar height profiles

The micropillar height profiles were deliberately selected to isolate and compare the effects of symmetry, periodicity, and directional asymmetry on passive micromixing under laminar flow conditions. The U configuration serves as a symmetric reference case, providing constant geometric obstruction along the flow direction and enabling baseline assessment of mixing induced by regularly spaced pillars without height modulation.

The HSW profile introduces periodic height variation along the flow direction, designed to promote repeated interface deformation and partial folding through alternating regions of increased and reduced pillar height. This configuration enables assessment of how periodic modulation of geometric confinement influences interface stretching and cumulative mixing.

The BST profile incorporates a monotonic, asymmetric height gradient aligned with the flow direction. This design was intended to impose a directional bias on the flow field, enhancing cumulative transverse displacement and interface distortion as the fluid progresses downstream. By comparing these three profiles within an identical

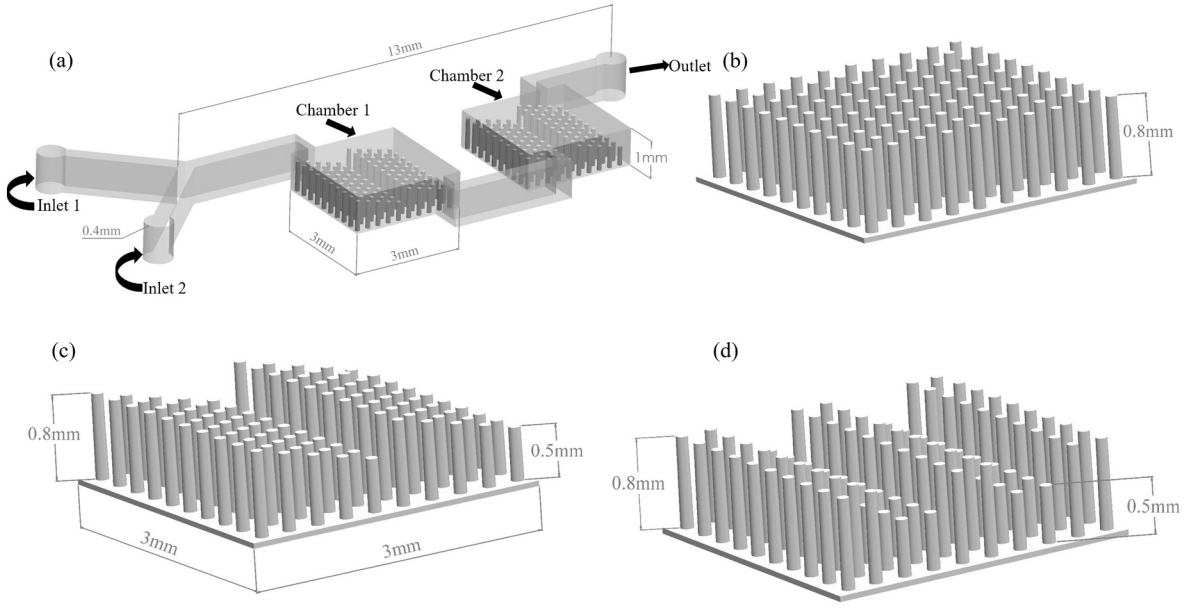


Fig. 1. Micromixers geometry and pillar configurations: (a) Three-dimensional schematic of the dual-inlet microfluidic micromixer comprising two successive micropillar array sections embedded in a straight microchannel; (b) Uniform (U) micropillar array with constant pillar height (c) Half-square-wave (HSW) micropillar array with stepwise pillar height variation (d) Backward sawtooth (BST) micropillar array with monotonic pillar height reduction from 0.8 mm to 0.5 mm.

channel layout, the design framework enables systematic evaluation of how spatial height variation and geometric asymmetry influence passive mixing efficiency.

2.3. Fabrication of height variable micropillars

A CO_2 laser system (Trotec Speedy 300, Trotec Laser GmbH, Marchtrenk, Austria) was used to fabricate U, HSW, and BST micropillar configurations in poly(methyl methacrylate) (PMMA). Variable machining depths for the HSW and BST designs were obtained by adjusting the laser power between 3.6 and 7.6 W, while maintaining a constant scan speed of 1 in. s^{-1} and a pulse frequency of 1000 PPI. Uniform pillars were fabricated at a fixed laser power of 7.6 W using the same speed and frequency conditions as before. A focal length of 2 in. was used for all configurations to achieve micropillars with a nominal diameter of 120 μm.

It should be noted that due to the CO_2 laser fabrication process, slight conical tapering was present at the micropillar tips. As all pillar-based configurations were fabricated under identical conditions, this geometric feature was consistent across designs and does not affect the comparative analysis of mixing performance.

Following machining, the PMMA substrates were cleaned in 1 M HCl and ultrasonicated for 5 min to remove residual debris prior to PDMS casting. The resulting micropillar arrays were subsequently bonded to the microchannels and used for experimental mixing characterisation.

2.4. Characterisation of micropillar height

The height profiles and surface morphology of the fabricated micropillar arrays were characterised prior to mixing experiments. Scanning electron microscopy (SEM) (Apreo 2, Thermo Fisher Scientific, Waltham, MA, USA) was used to examine pillar shape and array fidelity, while quantitative height measurements were obtained from colourimetric height maps and cross-sectional profiles.

Three-dimensional height maps were acquired using a laser scanning microscope (LEXT OLS5100, Olympus, Japan), from which pillar heights and spatial height variations were extracted. Cross-sectional height profiles were generated to confirm the intended height distributions for the uniform, half-square-wave, and backward sawtooth configurations.

2.5. Fabrication of micromixer with height-variable micropillars

Fig. 2 illustrates the fabrication process of the micromixer. A CO_2 laser engraver (Trotec Speedy 300) was used to ablate PMMA to produce master moulds for the channel and pillar features. The masters were cleaned by ultrasonication and with isopropanol to remove debris and surface contaminants before polymer casting. PDMS prepolymer (Sylgard 184) was poured onto the masters and degassed under vacuum to eliminate trapped air and ensure faithful replication of channel and pillar features. To facilitate demoulding for subsequent casts, the PMMA masters were silanised with trichloro(1H,1H,2H-perfluorooctyl) silane and lightly coated with silicone spray (WD-40). Before irreversible bonding, the PDMS layers were oxygen-plasma treated, rendering the microchannel surfaces temporarily hydrophilic and ensuring consistent wetting conditions during the experiments.

2.6. Experimental methodology and data analysis

The experimental set-up, shown in Fig. 3(c), consisted of the fabricated micromixer, two inlet syringes (10 mL, BD Plastics, Spain), a syringe pump (Shenchen, ISPLab02), an inverted epifluorescence microscope (Olympus IX3-HOS, Olympus Corporation, Japan), polymer tubing with an inner diameter of 1 mm (Adtech Polymer Engineering, UK), and a computer (Dell Latitude 5440). One inlet was supplied with a solution of fluorescein isothiocyanate (FITC, 0.257 mol m^{-3}) diluted in Milli-Q ultra-pure water (Milli-Q IQ 7000, Merck Millipore), while the second inlet was infused with Milli-Q ultra-pure water only. The fluids were delivered to the micromixer through the tubing. FITC was stored under the manufacturer's recommended conditions. A fresh working solution was prepared for each experiment to ensure consistency in fluorescence response. During experimentation and imaging, the solution was protected from ambient light and used at ambient laboratory temperature to minimise photobleaching and maintain measurement consistency.

Images of the mixing chambers were captured using a high-speed camera (Phantom, Vision Research) while varying the input flow rate from 0.72 mL h^{-1} to 72 mL h^{-1}, corresponding to Reynolds numbers

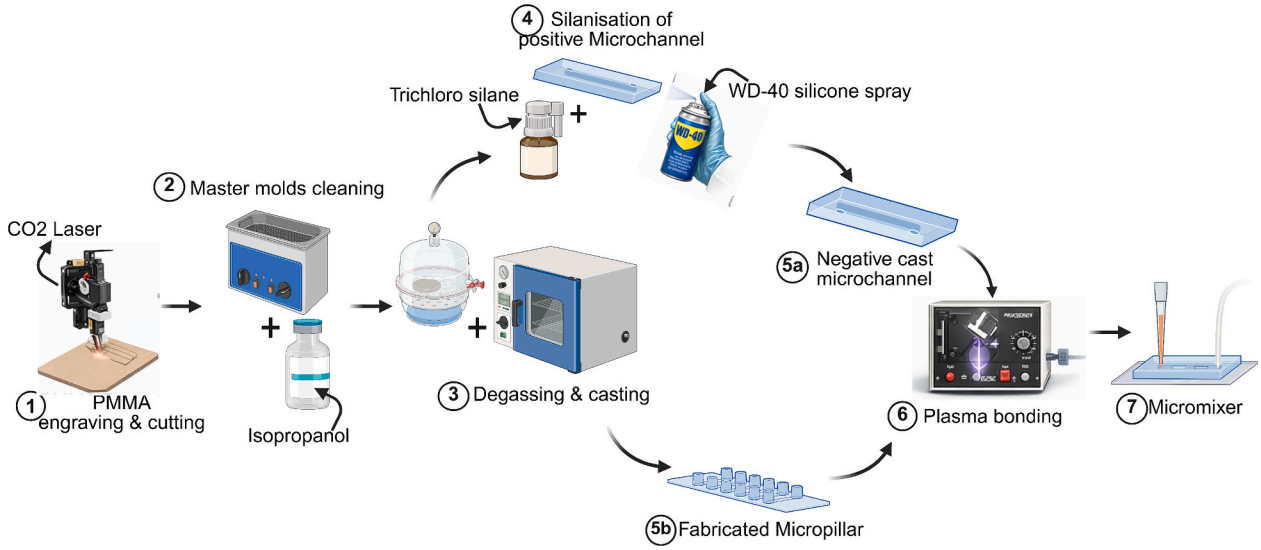


Fig. 2. Fabrication process of micromixer: PMMA master moulds defining channels and pillars were fabricated by CO_2 laser. The masters were ultrasonicated and rinsed with isopropanol before PDMS casting. PDMS was poured, degassed, cured, and silanised to enable demoulding. Negative microchannel replicas and separate micropillar arrays were produced and irreversibly bonded after oxygen plasma treatment to form the integrated micromixer. (Created in BioRender. Tanny, T. (2026) https://BioRender.com/na0a1ep).

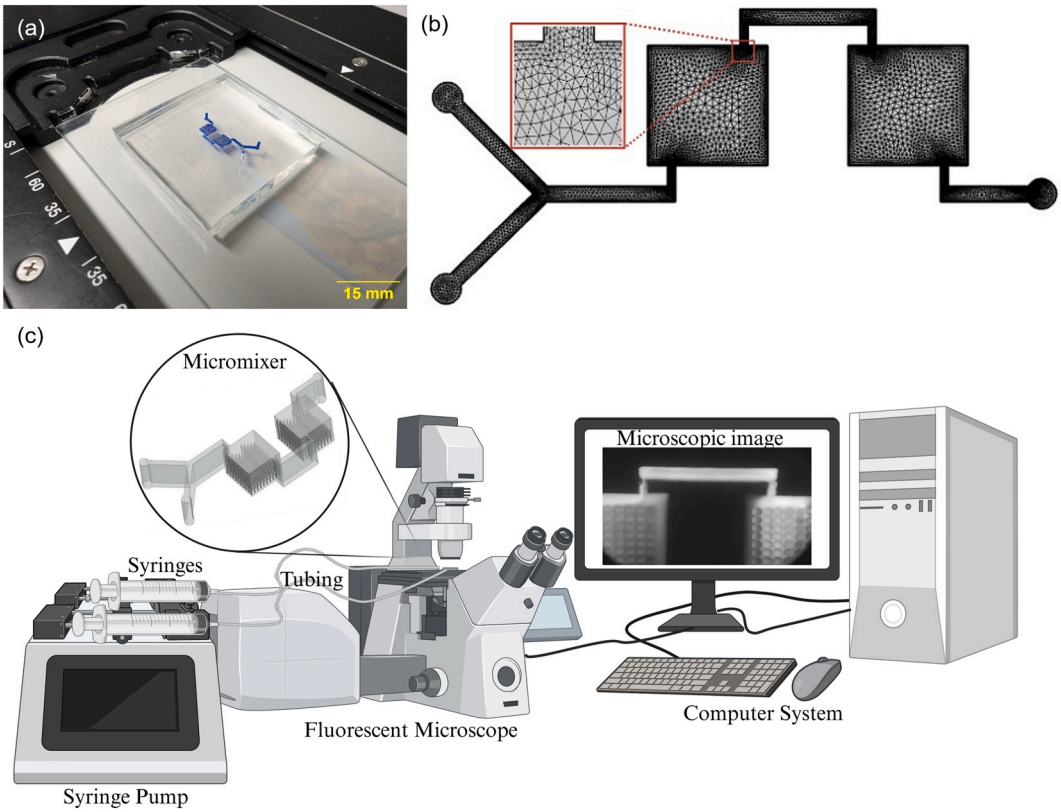


Fig. 3. Device realisation, internal microstructure, and experimental imaging setup (a) photograph of the fabricated micromixer mounted on the microscope stage; (b) Optical micrograph of the microchannel layout showing the mesh profile as used in numerical simulations; (c) Schematic of the experimental setup used for micromixing characterisation (Created in BioRender. Nejad, N. (2026) https://BioRender.com/p2j07z2.)

ranging from 0.1 to 10. The camera resolution was fixed at 2048 × 1536 pixels with an 8-bit greyscale depth and an exposure time of 100 μs.

The excitation and emission wavelengths of the filter cubes used for FITC imaging were 450–490 nm and 500–550 nm, respectively. The recorded images were subsequently analysed using ImageJ software (NIH, USA), and the extracted intensity values were used to calculate mixing efficiency and related performance metrics. Fig. 3(a) shows the fabricated micromixer, with the microchannels visualised using blue food dye. All experiments were performed in triplicate, and the resulting data were used for repeatability assessment and error analysis.

2.6.1. Flow characterisation and performance metrics

The inlet flows are laminar and characterised by the Reynolds number according to [31]:

$$Re = \frac{\rho u L}{\mu} = \frac{uL}{\nu} \tag{1}$$

$$L = \frac{4A}{P} \tag{2}$$

where ρ, μ, ν, u are density, dynamic viscosity, kinematic viscosity, and mean velocity; A is the cross-sectional area, P represents the wetted perimeter while L is the hydraulic diameter.

Mixing efficiency was determined from normalised fluorescence intensity measured at the outlet of each mixing chamber [32,33].

$$c^*_i = \frac{c_i - c_{min}}{c_{max} - c_{min}} \tag{3}$$

$$\sigma = \sqrt{\frac{1}{N}\sum_{i=1}^{N}(c^*_i - \overline{c^*})^2} \tag{4}$$

$$\eta = 1 - \frac{\sigma}{\sigma_{max}} \tag{5}$$

Here, c_i is the measured fluorescence intensity at sample point i, c_{min}, and c_{max} are the reference intensity values of the two unmixed inlet streams. c^*_i is the normalised intensity at sample point i, $\overline{c^*}$ is the mean normalised intensity, σ is the standard deviation of the normalised intensity distribution, σ_{max} is the standard deviation corresponding to the completely unmixed state, and N is the total number of samples. The mixing efficiency η ranges from 0, corresponding to an unmixed state, to 1, corresponding to complete mixing. In some studies, η is also referred to as the mixing index [27,34].

To quantify the relative enhancement in mixing performance due to the introduction of micropillars, an efficiency ratio (η_m) was defined as:

$$\eta_m = \frac{\eta_{mp}}{\eta_{NM}} \tag{6}$$

where η_{mp} and η_{NM} are the mixing efficiencies with micropillars and with no micropillars, respectively. Values of $\eta_m > 1$ indicate enhanced mixing due to micropillars, whereas values close to unity indicate little or no enhancement over the baseline design.

To account for both mixing performance and flow conditions, a performance index (PI) was defined as the ratio of mixing efficiency to Reynolds number [31]:

$$PI = \frac{\eta}{Re} \tag{7}$$

2.7. Numerical simulation

COMSOL Multiphysics was employed to carry out numerical analysis. The design described in Fig. 1 was imported into COMSOL and solved using two coupled physics interfaces, namely laminar flow and transport of diluted species, to model the fluid flow and mass transport of FITC and water, respectively. 2D simulations were carried out for the NM and U configurations. NM served as the baseline case without micropillars, while U represented the simplest micropillar-assisted design. These two cases provided a controlled comparison between a plain and a structured chamber, allowing the fundamental effect of micropillar inclusion on passive micromixing to be isolated and the numerical model to be validated against experimental results.

The experimental study, however, was conducted on all four configurations (NM, U, HSW, and BST) to evaluate the influence of micropillar geometry on mixing performance. The present work serves as an experimental proof-of-concept demonstrating that height variation can act as an additional geometric design parameter in micropillar-assisted passive micromixers. The HSW and BST designs were not included in the numerical analysis, as resolving their full flow-field characteristics would require detailed three-dimensional simulations capable of capturing arrangement-dependent transverse flow structures, local near-pillar advection, and species transport throughout the full two-chamber geometry. Such an analysis would substantially expand the scope of the work toward detailed CFD-based mechanistic modelling. Instead, the simulations were intended to establish a validated baseline, while the enhanced performance of HSW and BST is directly supported by experimental observations within the same platform. A more detailed three-dimensional flow-field analysis could provide further mechanistic insight into the local transport behaviour and transverse mixing characteristics of the height-variable configurations.

The outlet boundary was defined at zero-gauge pressure, while all channel walls were treated as no-slip boundaries. The fluid was assumed to be Newtonian, incompressible, and isothermal, with properties listed in Table 1.

The governing equations for incompressible, laminar, and Newtonian flow consist of the continuity equation and the Navier–Stokes Eqs. [35]:

$$\rho \nabla \bullet u = 0 \tag{8}$$

$$\rho \frac{\partial u}{\partial t} + \rho(u \bullet \nabla)u = \nabla \bullet [-PI + K] + F \tag{9}$$

$$K = \mu\left(\nabla u + (\nabla u)^T\right) \tag{10}$$

Here, u is the velocity vector, ρ is the fluid density, μ is the dynamic viscosity, P is the pressure, K is the viscous stress tensor, and F represents the external body forces.

The transport of diluted species was modelled using the advection–diffusion Eq. [35]:

$$\frac{\partial c_i}{\partial t} + \nabla \bullet j_i + u \bullet \nabla c_i = R_i \tag{11}$$

$$j_i = -D_i \nabla c_i \tag{12}$$

where, c_i is the concentration of the species involved (in this case FITC), D_i represents the diffusion coefficient, j_i is mass flux and u is the velocity field vector. The term $\frac{\partial c_i}{\partial t}$ is the rate of concentration with time, R_i represents the reaction term. As no chemical reactions occur in the present system, $R_i = 0$. The governing equation therefore accounts for advection by the flow field and molecular diffusion.

The numerical outputs were quantitatively analysed to evaluate the mixing efficiency and performance index. These numerical results were directly compared with experimental measurements for validation.

To ensure numerical reliability, a grid-independence study was conducted at $Re = 0.1$ on the NM configuration, the most diffusion-dominated condition considered in this work. Five progressively

Table 1
A summary of fluid properties [36] and the geometrical parameters.

Fluid properties		Geometrical parameters	
Density	998.2 kg/m^3	Pillar diameter	120 μm
Diffusion coefficient	4.86E-10 m^2/s	Pitch	300 μm
Dynamic Viscosity	1.002 mPa.s	Height range	500–800 μm
Inlet Concentration	0.257 mol m^{-3}	Inlet section length	2.88 mm
		Chamber depth without micropillar	200 μm
		Chamber depth with micropillar	1 mm
		Chamber area	3 mm × 3 mm
		Micromixer length	12 mm

refined meshes as shown in Fig. 3(b) were tested and summarised in Table 2, with the number of elements increasing from 105,803 to 194,603 and the number of nodes from 63,603 to 108,018. Across this refinement sequence, the mixing efficiency remained within 0.665–0.666, indicating minimal sensitivity to further mesh refinement. Following the Richardson extrapolation and Grid Convergence Index (GCI) procedure recommended by Celik et al. [37] and Roache [38], a three-grid convergence analysis was carried out using the Normal, Fine, and Finer meshes. The monitored concentration gave an apparent order of convergence of $p = 5.64$, an extrapolated value of 0.126573, a fine-grid convergence index of $GCI_{21} = 0.0198\%$ and a corresponding coarse-grid convergence index of $GCI_{32} = 0.0707\%$. The value of $GCI_{32}/r_{21}^{p} GCI_{21} = 1.0004$ was approximately unity, confirming asymptotic convergence. Although the difference between the Fine and Finer meshes was negligible, the Finer mesh was retained for all simulations to ensure maximum spatial resolution and minimise discretisation uncertainty near the micropillar regions. The same mesh strategy was then applied over $Re = 0.1–1$.

A time-step independence study was also performed using maximum time steps of 2.0, 1.0, 0.5, and 0.25 s at a final simulation time of 120 s. The corresponding mixing efficiencies were 0.6660, 0.6661, 0.6664, and 0.666, respectively, giving a maximum relative deviation of less than 0.1%. The numerical solution was therefore considered temporally independent, and a maximum time step of 0.5 s was adopted for all reported simulations.

3. Results and discussion

3.1. Validation of micropillar height profiles

The fabricated micropillar arrays were first examined to confirm that the realised height profiles matched the intended designs. Representative SEM images, three-dimensional height maps, and corresponding cross-sectional profiles for the U, HSW, and BST configurations are shown in Fig. 4.

The measured micropillar heights span approximately 500 μm to 820 μm, in good agreement with the target geometries. The U configuration exhibits a consistent pillar height across the array, while the HSW and BST configurations display the prescribed spatial height variations along the flow direction. These results confirm that the designed height profiles were successfully reproduced and provide a reliable basis for subsequent mixing performance comparisons.

3.2. Qualitative mixing behaviour: Experimental and numerical comparison

Qualitative mixing behaviour was examined experimentally for all four configurations (NM, U, HSW, and BST) and numerically for NM and U to establish a baseline and validate experimental observations. Fig. 5 presents representative experimental and numerical concentration fields for NM and U at $Re = 0.1$.

For the NM configuration (Fig. 5a), the two inlet streams remain largely unmixed, with a sharp and stable interface persisting across the chamber, indicating diffusion-dominated transport. In contrast, the U configuration (Fig. 5b) exhibits noticeable interface curvature and lateral spreading even at low Reynolds number, reflecting enhanced interface stretching induced by the presence of micropillars.

The corresponding numerical results (Fig. 5c and d) are consistent with the experimental observations. In the NM case, two segregated streams persist through Chamber 1, while in the U configuration mixing initiates primarily in Chamber 2, where cumulative flow perturbations become more pronounced. Although the flow remains laminar and near-symmetric, weak transverse motions and near-wall secondary flows increase interface deformation and promote enhanced interfacial contact, particularly in the downstream chamber. Supplementary Videos S1 (numerical) and S2 (experimental) illustrate the progressive downstream homogenisation across the full device length.

Overall, the close agreement between experimental observations and numerical predictions confirms that geometry-induced flow perturbations govern the observed mixing behaviour and supports the use of numerical simulations to interpret and extend the experimental findings.

Table 2
A summary of Mesh properties for Grid convergence test.

Mesh Type	No. of Elements	No. of Nodes	Min. element size	Max. element size	Mixing Index
Coarser	105,803	63,603	0.0293	0.638	0.6659
Coarse	140,094	80,749	0.022	0.492	0.6662
Normal	167,383	94,396	0.0147	0.33	0.6652
Fine	175,130	98,270	0.00734	0.257	0.6658
Finer	194,603	108,018	0.00293	0.205	0.6660

3.3. Mixing efficiency evaluation in chambers 1 and 2

Fig. 6 summarises the experimentally measured mixing efficiencies for NM, U, HSW, and BST in Chambers 1 and 2 over the Reynolds number range $Re = 0.1–10$, together with two-sided 95% confidence intervals. Here, the mixing efficiency at each chamber was evaluated from the local concentration field measured at the corresponding chamber outlet section. Accordingly, the Chamber 2 value represents the cumulative mixing state after the fluid has passed through the upstream part of the device, rather than the mixing generated within Chamber 2 in isolation.

In Chamber 1, NM shows the lowest mixing efficiency across the entire Reynolds number range. It decreases from about 0.64 to at $Re = 0.1$ to about 0.53 at $Re = 1$ and remains below 0.60 at higher Reynolds numbers. This shows that mixing remains limited when it depends solely on diffusion, with no geometric disturbance introduced. Adding uniform-height pillars (U) significantly improves mixing at low Reynolds numbers, reaching about 0.80 at $Re = 0.1$. However, because the U arrangement is geometrically symmetric, it cannot sustain strong transverse motion, and the mixing efficiency gradually decreases as the Reynolds number increases.

The HSW configuration provides further improvement by breaking symmetry and introducing periodic height modulation. In Chamber 1, HSW reaches a mixing efficiency of approximately 0.84 at Re = 0.1 and remains above 0.70 over the full Reynolds number range. The repeated height variation enhances interface stretching and flow reorganisation more effectively than the uniform-height configuration. BST shows the highest mixing efficiency in Chamber 1 across $Re = 0.1–10$. At Re = 0.1, BST reaches approximately 0.86, reflecting its asymmetric height profile. The backward-facing geometry locally disturbs the laminar stream, generating transverse motion and localised shear that intensify interfacial deformation. Mixing efficiency remains above 0.70 even at higher Reynolds numbers.

In Chamber 2, the mixing efficiency is higher for all configurations because the fluid has undergone further downstream transport before reaching that section. NM remains the weakest configuration, but its mixing efficiency is higher than in Chamber 1, reaching about 0.72 at $Re = 1$. The U configuration shows a modest improvement at low Reynolds numbers, but this improvement decreases as inertia increases. Both HSW and BST maintain high mixing efficiencies in Chamber 2, with HSW reaching about 0.89–0.97 for $Re < 1$. BST gives the best overall performance, peaking at about 0.98 near $Re \approx 0.9$ and remaining above 0.70 across the entire Reynolds number range. These results show that the downstream section benefits from continued advection–diffusion and further interface development, with the greatest improvement observed for the height-variable asymmetric geometries.

Compared with earlier micropillar-assisted passive micromixers, the

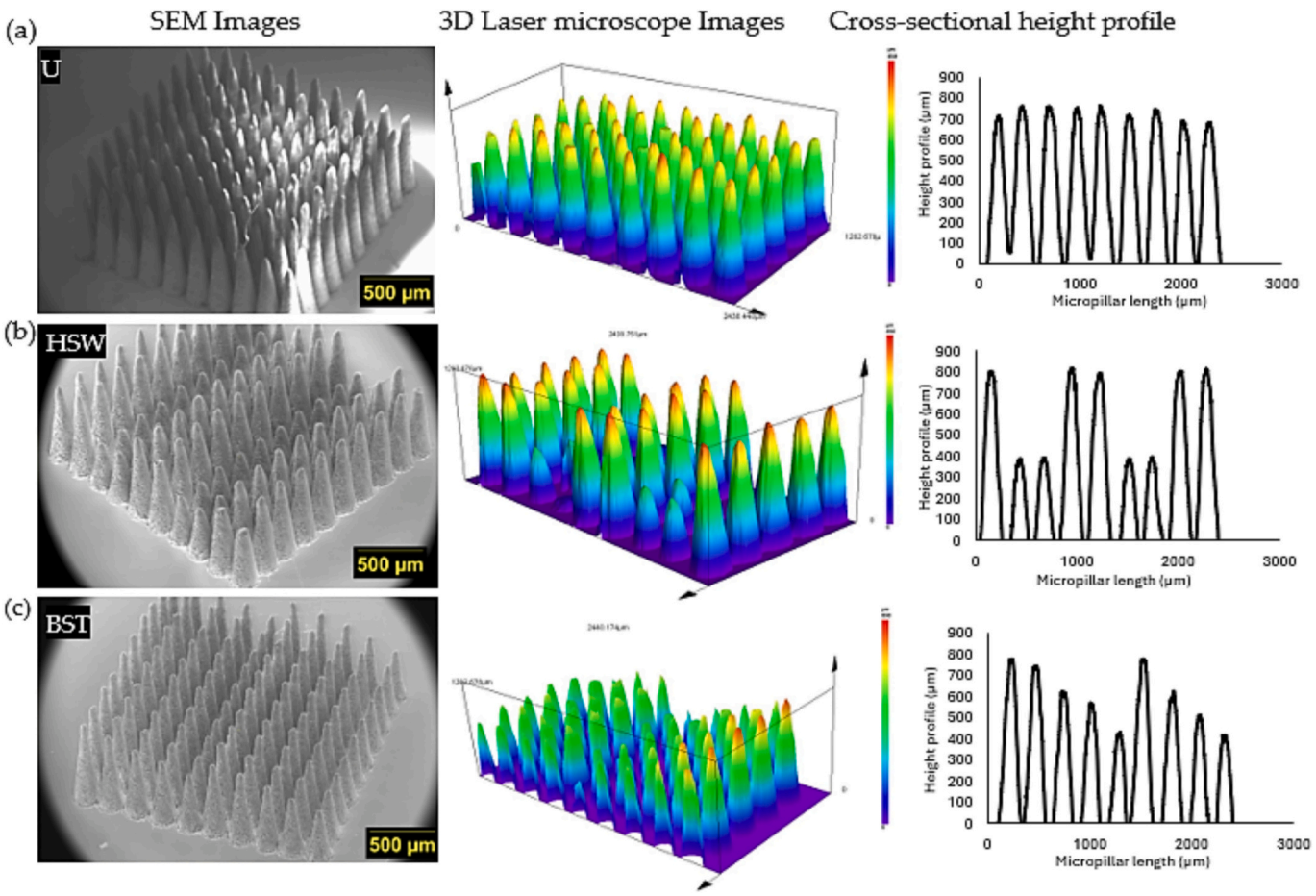


Fig. 4. Validation of fabricated micropillar height profiles. SEM images, three-dimensional height maps, and corresponding cross-sectional height profiles of (a) U, (b) HSW, and (c) BST configurations.

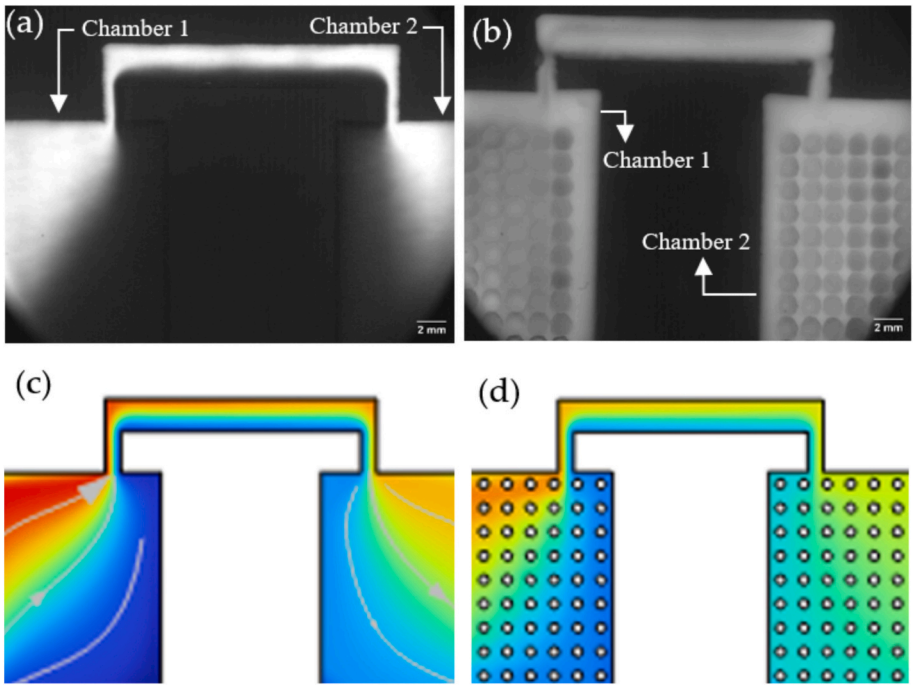


Fig. 5. Concentration profiles of NM and U (a) Gray scale image of NM at $Re = 0.1$ (b) Gray scale image of U at $Re = 0.1$. (c) A close-up view of the numerical simulation concentration profile of NM at $Re = 0.1$ (d) A close-up view of the numerical simulation concentration profile of U at $Re = 0.1$.

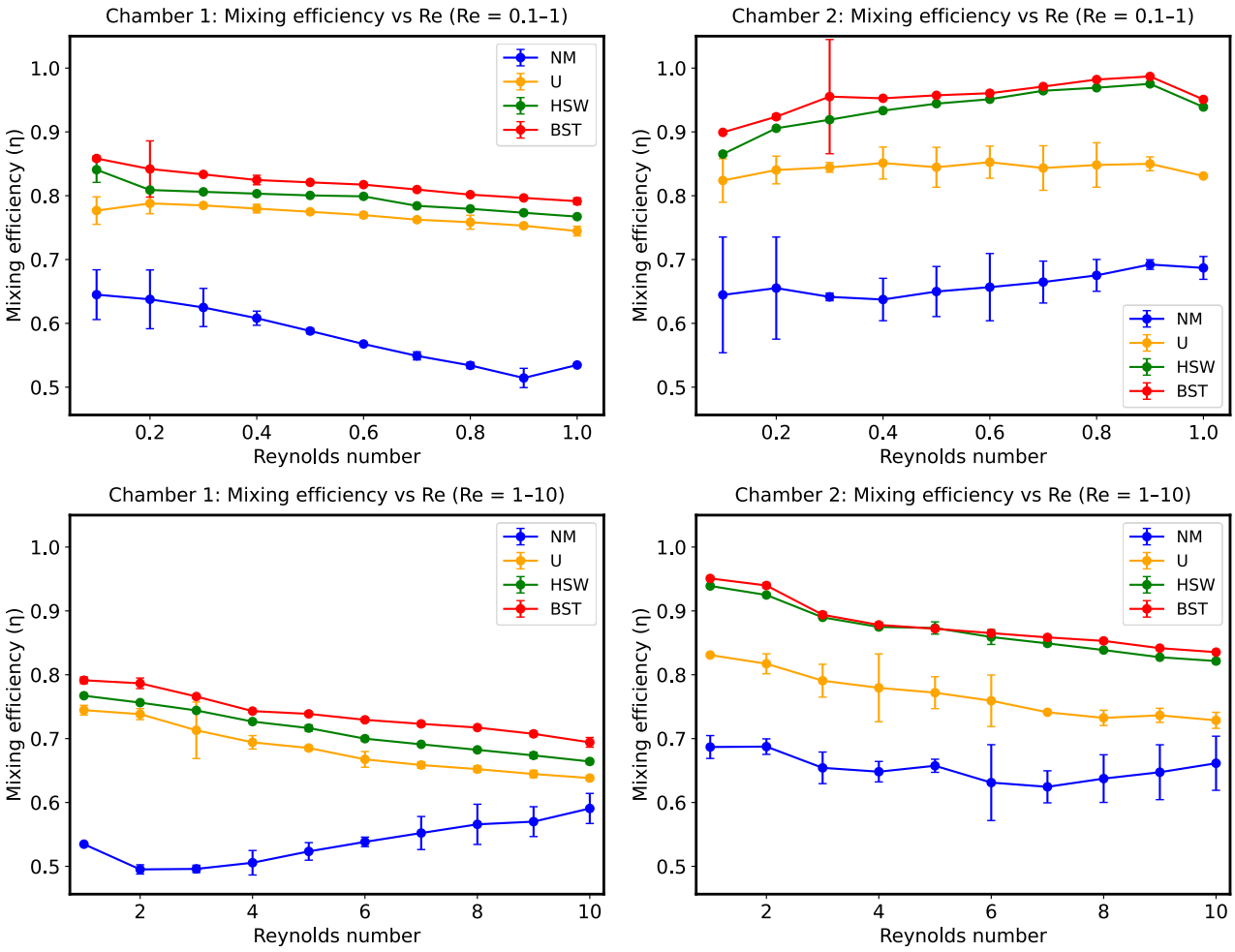


Fig. 6. Mixing efficiency as a function of Reynolds number for the no-micropillar channel (NM), uniform (U), half-square-wave (HSW), and backward-sawtooth (BST) micropillar configurations in Chamber 1 (left panels) and Chamber 2 (right panels). The upper panels correspond to the low-*Re* regime (*Re* = 0.1–1), while the lower panels show the moderate-*Re* regime (*Re* = 1–10). Error bars highlight the standard deviation obtained from repeated measurements.

present results show that the improvement comes not only from adding micropillars, but from combining height variation and asymmetry within a single platform. In the present work, BST consistently outperformed NM, U, and HSW in both chambers, achieving an experimental mixing efficiency of about 98% at Re ≈ 0.9 in Chamber 2, and yielding the highest efficiency ratio and performance index under the same operating conditions. Earlier studies have shown that micropillar arrangement, spacing, and obstacle geometry strongly influence interfacial deformation and transverse transport. Barzoki et al. [39] reported mixing indices up to 99.5% in optimised pillar-based passive micromixers. Still, their study focused mainly on pillar configuration and gap effects within a numerical framework rather than on height-variable asymmetric arrays examined experimentally within a single common platform. Tran-Minh et al. [40] reported strong laminar mixing using ellipse-like planar micropillars. At the same time, Antognoli et al. [27] showed that pre-arranged micropillar sequences can improve passive mixing for fluids with different properties. However, those studies did not separately examine the effect of pillar-height variation combined with the geometric asymmetry considered in the present work.

In this context, the present results indicate that the superior performance of BST arises from stronger downstream flow redistribution, interfacial stretching, and transverse transport relative to both the uniform and pillar-free references and are further supported by direct experimental validation.

The uncertainty analysis shows that these trends are consistent. The U, BST, and HSW configurations have small confidence intervals across the Reynolds number range studied, thereby showing good repeatability of the measurements. In contrast, NM shows greater variation, especially in Chamber 2 under low-Re conditions. Even so, the uncertainty does not change the performance ranking, with BST and HSW consistently performing better than U and NM in both chambers.

3.4. Quantitative mixing behaviour: Experimental and numerical comparison

Experimental results were quantitatively compared with numerical simulations for NM and U in the low-Reynolds-number regime (*Re* = 0.1–1), where the highest mixing efficiencies were observed in both chambers. Fig. 7 presents the corresponding experimental and numerical mixing efficiencies for Chambers 1 and 2.

In Chamber 1 (Fig. 7a), both experimental and numerical results show a monotonic decrease in mixing efficiency with increasing Reynolds number for NM and U. This trend reflects the reduction in residence time and the diminishing role of molecular diffusion as the flow rate increases. The numerical simulations capture the overall trend well. For U, the simulations slightly underpredict the experimental values at higher Reynolds numbers, which can be attributed to the simplified representation of micro-scale vortical structures and streamline curvature effects that contribute to enhanced advection in the experiments. For NM, the numerical model shows close agreement across the range, with only minor deviations at intermediate Reynolds numbers.

In Chamber 2 (Fig. 7b), both experimental and numerical results

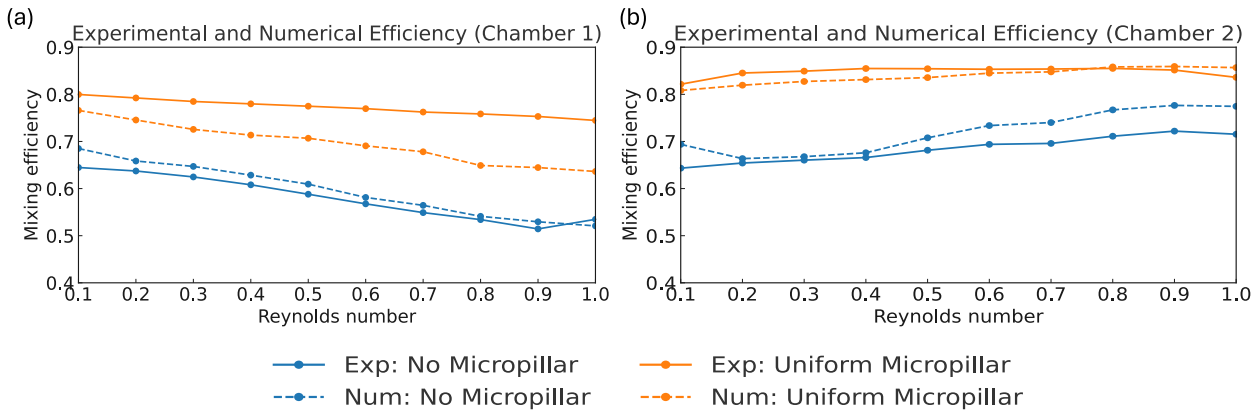


Fig. 7. Comparison of experimental and numerical mixing efficiencies for NM and U in (a) Chamber 1 and (b) Chamber 2 over the Reynolds number range $Re = 0.1–1$.

exhibit a gradual increase in mixing efficiency with Reynolds number for NM and U. This behaviour is consistent with cumulative advection and geometry-induced flow redistribution in the downstream chamber. The numerical predictions reproduce this increasing trend with good fidelity. Minor discrepancies between simulations and experiments are observed at the lowest and highest Reynolds numbers but do not alter the overall agreement or the relative performance between configurations.

Overall, the close correspondence between experimental measurements and numerical predictions across both chambers demonstrates that the numerical model captures the dominant transport mechanisms governing mixing in the micromixer. The agreement supports the use of the present modelling framework as a reliable quantitative tool for interpreting experimental trends and for pre-experimental screening of micromixer designs in the low-Reynolds-number regime.

3.5. *Efficiency ratio analysis*

The efficiency ratio, η_m, defined by Eq. (6) in Section 2.6.1, was used to measure the relative improvement in mixing produced by the micropillars compared with the no-pillar baseline under the same flow conditions. Values of $\eta_m > 1$ indicate enhanced mixing due to geometric structuring.

Fig. 8 presents the efficiency ratios for U, HSW, and BST in Chambers 1 and 2 over the Reynolds number ranges $Re = 0.1–1$ and $Re = 1–10$. In the diffusion-dominated regime (Re = 0.1–1), all micropillar configurations exhibit efficiency ratios exceeding unity, confirming that geometric modulation significantly enhances mixing at low Reynolds numbers. In Chamber 1, BST consistently achieves the highest efficiency ratios, reaching values of approximately 1.5–1.55, followed by HSW, while U provides the smallest relative enhancement. This ordering reflects the increasing degree of height variation and geometric asymmetry among the designs.

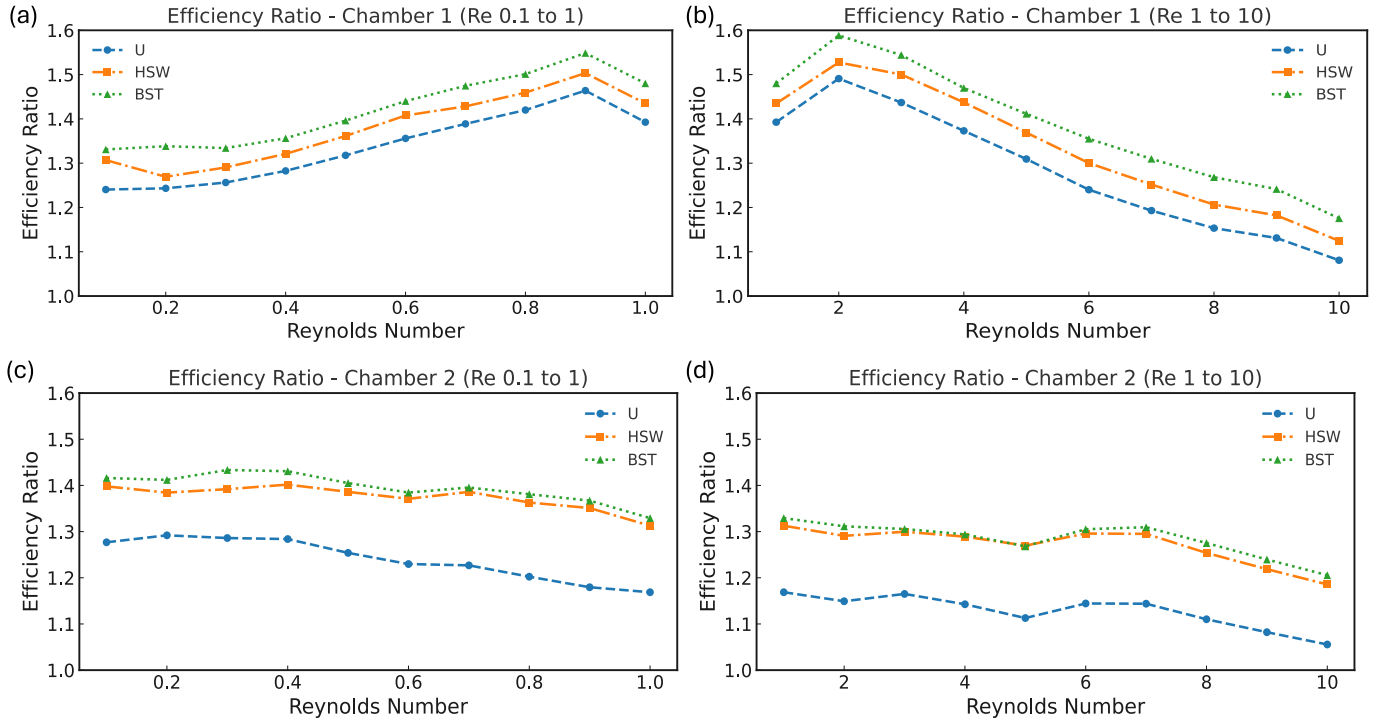


Fig. 8. Efficiency ratio as a function of Reynolds number for the uniform (U), half-square-wave (HSW), and backward-sawtooth (BST) micropillar configurations in (a, b) Chamber 1 and (c, d) Chamber 2. Panels (a) and (c) correspond to the low-*Re* regime ($Re = 0.1–1$), while panels (b) and (d) show the moderate-*Re* regime ($Re = 1–10$).

In Chamber 2, efficiency ratios are generally lower than in Chamber 1 but remain above unity for all micropillar configurations in the low-Re regime. BST and HSW exhibit comparable enhancement levels, whereas U shows more modest gains. The reduced relative enhancement in Chamber 2 is attributed to the higher baseline mixing already achieved downstream, which limits the incremental benefit of additional geometric perturbations.

As Reynolds number increases into the moderate-Re regime (Re = 1–10), efficiency ratios decrease gradually in both chambers, indicating a reduced relative influence of geometry-driven mixing as inertia-induced secondary flows become more prominent. Nevertheless, BST maintains the highest efficiency ratios across the entire Reynolds number range, remaining above approximately 1.3 in Chamber 1 and above approximately 1.2 in Chamber 2. In contrast, HSW trends toward unity at higher Reynolds numbers, while U consistently exhibits the weakest enhancement.

Overall, the efficiency-ratio analysis highlights the strong sensitivity of low-*Re* micromixing performance to micropillar height variation and geometric asymmetry. Among the investigated designs, BST provides the most robust and persistent enhancement across both chambers and across all Reynolds numbers considered, reinforcing the effectiveness of asymmetric, height-graded micropillar profiles for passive micromixing.

3.6. Performance index evaluation

Fig. 9 shows the performance index (PI) for NM, U, HSW, and BST in Chambers 1 and 2 over the Reynolds number range *Re* = 0.1–10. Since PI accounts for both mixing efficiency and flow conditions, it reflects the mixing performance per unit Reynolds number.

At Re = 0.1–1, PI reaches its highest values across all configurations. This shows that viscous effects and diffusion-assisted transport govern the flow in this regime. In Chamber 1, BST records the highest performance index (PI), reaching approximately 8.5 at Re = 0.1, followed by HSW and U. By contrast, NM gives the lowest PI, owing to weak advection and limited interfacial stretching. This pattern follows the increasing degree of height variation and geometric asymmetry introduced across the designs.

In Chamber 2, PI values remain consistently higher than those in Chamber 1 throughout the low-Re regime. BST again yields the highest PI, reaching about 9.0 at *Re* = 0.1, while HSW and U show comparable performance. NM remains the least effective configuration. The enhanced PI in Chamber 2 reflects the combined effect of downstream development length and geometry-induced transverse transport, which together promote more efficient utilisation of viscous mixing mechanisms.

As Reynolds number increases into the moderate-Re regime (Re = 1–10), PI decreases rapidly for all configurations and converges to values in the range of approximately 0.05–0.75. This convergence suggests that, as inertial effects increase, diffusion becomes insignificant and PI becomes less sensitive to geometric modulation. Nevertheless, BST consistently retains the highest PI in both chambers, indicating superior mixing performance per unit flow cost across the entire Reynolds number range.

Overall, the PI analysis shows that micropillar-based designs are most advantageous at low *Re*, where viscous effects dominate. Among the configurations investigated, BST provides the best balance between mixing enhancement and flow conditions, while Chamber 2 consistently delivers better performance due to the cumulative effect of its geometry. The superiority of BST in the present study is established relative to NM, U, and HSW within the same micromixer platform. A direct comparison of pressure drop or energy consumption at equivalent mixing efficiency is not included in the present study, as the focus is on isolating the effect of micropillar geometry on mixing performance; however, the performance index provides a consistent basis for assessing the balance between mixing effectiveness and operating conditions across the investigated configurations.

4. Conclusion

Efficient fluid mixing remains a fundamental challenge in

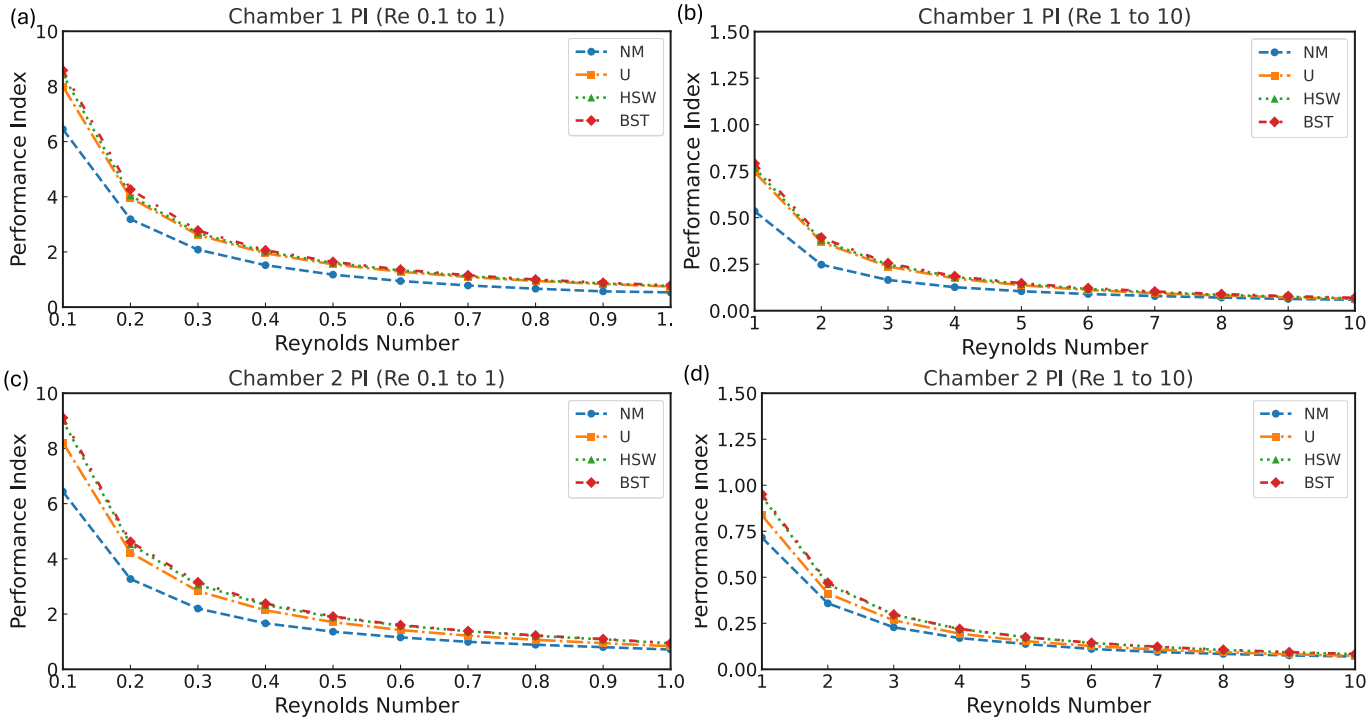


Fig. 9. Performance index (PI) as a function of Reynolds number for the no-micropillar (NM), uniform (U), half-square-wave (HSW), and backward-sawtooth (BST) configurations in (a, b) Chamber 1 and (c, d) Chamber 2. Panels (a) and (c) correspond to the low-*Re* regime (*Re* = 0.1–1), while panels (b) and (d) show the moderate-*Re* regime (*Re* = 1–10).

microfluidic systems, where laminar flow and diffusion-limited transport dominate at low Reynolds numbers. In this study, passive micromixing was systematically investigated using a no-pillar baseline (NM) and three micropillar configurations with systematically increasing height variation along the flow direction (U, HSW, and BST), combining experiments and numerical simulations over Re = 0.1–10.

Asymmetric-height micropillar arrays were found to significantly improve mixing by increasing streamline curvature, interfacial stretching, and transverse transport. Among the investigated designs, the BST configuration consistently delivered the highest mixing performance in the two chambers across the entire Reynolds number range. The advantage of BST was particularly evident in the diffusion-dominated regime, where it achieved experimental mixing efficiencies of about 98%, with the highest efficiency ratios and performance indices. These results indicate that geometric asymmetry and monotonic height variation are particularly effective in sustaining mixing under viscous constraints.

Across all configurations, the downstream chamber exhibited superior performance due to cumulative hydrodynamic development and enhanced advection–diffusion coupling. While the relative contribution of geometric modulation diminished at higher Reynolds numbers as inertial effects became more prominent, the ordering of performance (BST $\gtrsim$ HSW $>$ U $\gg$ NM) was preserved. The performance index analysis further confirmed that micropillar-based designs, and BST in particular, offer superior mixing performance per unit flow condition, especially at low Reynolds numbers. In the present study, Newtonian fluids were used to isolate the effect of micropillar geometry on passive micromixing under controlled conditions. As non-Newtonian fluids may exhibit shear-dependent viscosity and viscoelastic behaviour, their mixing response may differ from that reported here. The applicability of the proposed designs to non-Newtonian systems remains an important extension of this work, particularly for biomedical and chemical-processing applications.

Overall, this work establishes asymmetric micropillar arrays as a robust and energy-efficient strategy for passive micromixing. The BST design provides a versatile platform for low-Re microfluidic applications that require efficient mixing without external actuation. Future integration of such geometries with on-chip sensing, reaction, or responsive materials may enable adaptive microfluidic systems with enhanced transport, reaction efficiency, and analytical sensitivity for lab-on-a-chip and point-of-care technologies.

CRediT authorship contribution statement

Azeez Bakare: Writing – original draft, Visualization, Validation, Software, Methodology, Data curation. **Prabuddha De Saram:** Methodology, Investigation, Data curation. **Hongjie An:** Writing – review & editing, Supervision. **Nam-Trung Nguyen:** Writing – review & editing, Supervision, Resources, Project administration, Formal analysis. **Navid Kashaninejad:** Writing – review & editing, Writing – original draft, Supervision, Resources, Investigation, Funding acquisition, Formal analysis, Conceptualization.

Funding

This research was funded by the Australian Research Council (ARC) Discovery Early Career Research Award (DECRA) (DE220100205).

Declaration of competing interest

The authors declare that they have no known competing financial interests or personal relationships that could have appeared to influence the work reported in this paper.

Acknowledgments

This work used the Queensland node of the NCRIS-enabled Australian National Fabrication Facility (ANFF).

Appendix A. Supplementary data

Supplementary data to this article can be found online at https://doi.org/10.1016/j.cej.2026.177622.

Data availability

Data will be made available on request.

References

[1] John A. Davis, D.W.I., Keith J. Morton, David A. Lawrence, Lotien R. Huang, Stephen Y. Chou, James C. Sturm, Robert H. Austin, Deterministic hydrodynamics: taking blood apart, Proc. Natl. Acad. Sci. USA 103 (40) (2006) 14779–14784.
[2] M. Ebadi, et al., A tool for designing tree-like concentration gradient generators for lab-on-a-chip applications, Chem. Eng. Sci. 212 (2020) 115339.
[3] L. Chen, et al., Porous structural microfluidic device for biomedical diagnosis: a review, Micromachines 14 (3) (2023) 547.
[4] S.A. Jaywant, K.M. Arif, A comprehensive review of microfluidic water quality monitoring sensors, Sensors 19 (21) (2019) 4781.
[5] M. Bayareh, M.N. Ashani, A. Usefian, Active and passive micromixers: a comprehensive review, Chem. Eng. Process. Process Intensif. 147 (2020).
[6] W. Raza, S. Hossain, K.-Y. Kim, A review of passive micromixers with a comparative analysis, Micromachines 11 (2020) 455, https://doi.org/10.3390/mi11050455.
[7] M. Rismanian, M.S. Saidi, N. Kashaninejad, A new non-dimensional parameter to obtain the minimum mixing length in tree-like concentration gradient generators, Chem. Eng. Sci. 195 (2019) 120–126.
[8] S. Kim, et al., Monolithic 3D micromixer with an impeller for glass microfluidic systems, Lab Chip 20 (23) (2020) 4474–4485.
[9] B. Mondal, S. Pati, P.K. Patowari, Fabrication of wavy micromixer using soft lithography technique, Mater. Today Proc. 26 (2020) 1271–1278.
[10] L. Lin, C.-K. Chung, PDMS Microfabrication and Design for Microfluidics and Sustainable Energy Application: Review, Micromachines 12 (11) (2021) 1350.
[11] A. Agha, A. Alazzam, E. Abu-Nada, Acoustofluidic polymer micropillars for efficient micromixing and nanoparticle synthesis, Int. J. Eng. Sci. 219 (2026) 104430.
[12] H. Ammar, et al., Enhanced micromixer designs for chemical applications – numerical simulations and analysis, Chem. Eng. Process. 208 (2025).
[13] S. Chen, et al., Design, evaluation, and optimization of a new micromixer based on three-dimensional multilaminar flow, Chem. Eng. Res. Des. 214 (2025) 105–113.
[14] Y. Zheng, et al., Mixing performance analysis and optimal design of a novel passive baffle micromixer, Micromachines 15 (2) (2024) 182.
[15] M. Juraeva, D.-J. Kang, Design and Mixing Analysis of a Passive Micromixer with Circulation Promoters, Micromachines 15 (7) (2024) 831.
[16] R.E. Pawinanto, J. Yunas, A.M. Hashim, Micropillar based active microfluidic mixer for the detection of glucose concentration, Microelectron. Eng. 234 (2020).
[17] X. Chen, J. Shen, Design and Simulation of a Chaotic Micromixer with Diamond-Like Micropillar Based on Artificial Neural Network, Int. J. Chem. React. Eng. 15 (2) (2017).
[18] A.D. Stroock, et al., Chaotic mixer for microchannels, Science 295 (5555) (2002) 647–651.
[19] M.A. Ansari, K.-Y. Kim, Shape optimization of a micromixer with staggered herringbone groove, Chem. Eng. Sci. 62 (23) (2007) 6687–6695.
[20] W. Raza, S. Hossain, K.Y. Kim, A Review of Passive Micromixers with a Comparative Analysis, Micromachines (Basel) 11 (5) (2020).
[21] T. Peng, et al., Investigation of geometric modifications in T-type micromixers for enhanced microfluidic mixing and ZIF-8 synthesis, Results Eng. 26 (2025).
[22] S.F. Javed, et al., Performance analysis of three-dimensional passive micromixers using k-means priority clustering with AHP-based sustainable design optimization, Sci. Rep. 15 (1) (2025) 18140.
[23] B. Yuan, S. Yuan, H. Wang, Numerical and Experimental Investigation of Mixing Enhancement in a Zigzag Passive Micromixer with D-Shaped Obstacles, Micromachines (Basel) 17 (2) (2026).
[24] K. Chen, et al., Mixing enhancement of a novel C-SAR microfluidic mixer, Chem. Eng. Res. Des. 132 (2018) 338–345.
[25] Z. Zhou, et al., Investigation of mixing characteristics in a novel SAR micromixer with locally overlapping V-shaped flow channels, Chem. Eng. Process. 195 (2024).
[26] A. Kheirkhah Barzoki, Optimization of passive micromixers: effects of pillar configuration and gaps on mixing efficiency, Sci. Rep. 14 (1) (2024) 16245.
[27] M. Antognoli, et al., Pre-arranged sequences of micropillars for passive mixing control of water and ethanol, Chem. Eng. J. 461 (2023).
[28] O.E. Strom, J.P. Beech, J.O. Tegenfeldt, Geometry-Dependent Elastic Flow Dynamics in Micropillar Arrays, Micromachines 15 (2) (2024).
[29] M. Waqas, et al., The Design and Investigation of Hybrid a Microfluidic Micromixer, Appl. Sci. 14 (12) (2024).

[30] J. Li, et al., Design and optimization of Tesla micromixer with asymmetrical arrangement for efficient mixing in microfluidic chip, Chem. Eng. Process. 209 (2025).
[31] A. Najafpour, et al., Numerical study of mixing performance in T-junction passive micromixer with twisted design, Chem. Eng. Process. 194 (2023).
[32] N.-T. Nguyen, Characterization techniques, in: Micromixers, 2012, pp. 295–320.
[33] H. Fu, X. Liu, S. Li, Mixing indexes considering the combination of mean and dispersion information from intensity images for the performance estimation of micromixing, RSC Adv. 7 (18) (2017) 10906–10914.
[34] M. Waqas, et al., Design and investigation of a passive-type microfluidics micromixer integrated with an Archimedes screw for enhanced mixing performance, Micromachines 16 (1) (2025) 82.
[35] R.R. Lopez, et al., Numerical and Experimental Validation of Mixing Efficiency in Periodic Disturbance Mixers, Micromachines 12 (9) (2021).
[36] G. Wypych, PDMS polydimethylsiloxane, ChemTec Publishing, 2016, pp. 340–344.
[37] Procedure for Estimation and Reporting of Uncertainty Due to Discretization in CFD Applications, J. Fluids Eng. 130 (7) (2008).
[38] P.J. Roache, Verification and Validation in Computational Science and Engineering, Hermosa Publishers, 1998.
[39] A. Kheirkhah Barzoki, Optimization of passive micromixers: effects of pillar configuration and gaps on mixing efficiency, Sci. Rep. 14 (1) (2024) 16245.
[40] N. Tran-Minh, T. Dong, F. Karlsen, An efficient passive planar micromixer with ellipse-like micropillars for continuous mixing of human blood, Comput. Methods Prog. Biomed. 117 (1) (2014) 20–29.